Atmospheric
Measurement
Techniques
Discussions

Open Access

EGU

Rayleigh wind retrieval for the ALADIN airborne demonstrator of the Aeolus mission using simulated response calibration

Xiaochun Zhai[1,2], Uwe Marksteiner[1], Fabian Weiler[1], Christian Lemmerz[1], Oliver Lux[1], Benjamin Witschas[1], Oliver Reitebuch[1]

5 [1]Deutsches Zentrum für Luft- und Raumfahrt e.V. (DLR), Institut für Physik der Atmosphäre,

Oberpfaffenhofen 82234, Germany

[2]Ocean University of China, College of Information Science and Engineering, Ocean Remote Sensing Institute,

Qingdao 266100, China

Correspondence to: Oliver. Reitebuch (Oliver.Reitebuch@dlr.de)

10 **Abstract.** Aeolus, launched on August 22nd in 2018, is the first ever satellite to directly observe wind information from the surface up to 30 km on a global scale. An airborne prototype called ALADIN Airborne Demonstrator (A2D) was developed at the German Aerospace Centre (DLR) for validating the Aeolus measurement principle based on realistic atmospheric signals. To obtain accurate wind retrievals, the A2D uses a measured Rayleigh response calibration (MRRC) to calibrate its Rayleigh channel signals. However, the atmospheric and instrumental variability currently limit the reliability and repeatability

15 of this MRRC. Thus, a procedure for a simulated Rayleigh response calibration (SRRC) is developed and presented in this paper to resolve these limitations of the A2D Rayleigh channel MRRC. The transmission functions of the A2D Rayleigh channel interferometer, consisting of the double-edge Fabry-Perot interferometers (FPIs), are firstly characterised and optimized based on measurements performed during different airborne and ground-based campaigns. The optimized FPI transmission function is then combined with the molecular Rayleigh backscatter spectrum to derive an accurate A2D SRRC

20 which can finally be implemented in the A2D wind retrieval. Using dropsonde data as a reference, a statistical analysis based on data from a flight campaign in 2016 reveals a bias and a standard deviation of line-of-sight (LOS) wind speeds derived from an SRRC of only 0.05 m s^{-1} and 2.52 m s^{-1}, respectively. Compared to the result derived from a MRRC with a bias of 0.23 m s^{-1} and a standard deviation of 2.20 m s^{-1}, the accuracy improved while the precision is considered to be at the same level. Furthermore, it is shown that SRRC allows the simulation of receiver responses over the whole altitude range from the

25 aircraft down to sea level, thus overcoming limitations due to continuous ground elevation during the performance of airborne instrument response calibrations.

1 Introduction

Continuous global wind observations are of highest priority for improving the accuracy of numerical weather prediction as well as for advancing our knowledge of atmospheric dynamics (Stoffelen et al., 2005; Weissmann et al., 2007; Žagar et al., 2008; Baker et al., 2014). Among the various techniques such as radiosonde, radar wind profiler, and geostationary satellite

5   imagery, a spaceborne Doppler wind lidar is considered as the most promising one to meet the need of near-real time observations of global wind information. Based on the principle of the Doppler effect, two different wind lidar detection techniques, namely coherent and direct detection, have been developed and studied over the last decades (Stoffelen et al., 2005; Reitebuch, 2012). The coherent Doppler lidar (CDL), typically used in the particle-rich boundary layer, can directly determine the Doppler frequency shift via the beat signal between the emitted laser signal and the particulate backscattered light. This is

10 different for a direct detection wind lidar, where the measured signal cannot be directly related to the frequency shift. Thus, a response calibration describing the relationship between the response and the Doppler frequency shift constitutes a prerequisite for accurate wind retrieval. The direct detection wind lidar can measure atmospheric wind by means of either particulate or molecular backscatter signals, typically offering much higher data coverage of the wind field from ground up to the lower mesosphere. Different spectral discriminators such as Fabry-Perot interferometers (Chanin et al., 1989; Korb et al., 1992),

15 Fizeau interferometers (McKay, 1998; McKay, 2002), iodine vapor filters (Liu et al., 2002; She et al., 2007;Baumgarten, 2010; Wang et al., 2010; Hildebrand et al., 2012), Michelson interferometers (Thuillier et al., 1991; Herbst et al., 2016) and Mach-Zehnder interferometers (Bruneau, 2001; Bruneau and Pelon, 2003; Tucker et al., 2018) can be used for direct detection wind lidars.

Aeolus, launched on August 22nd, 2018, is the first ever satellite to directly observe line-of-sight (LOS) wind profiles on a

20 global scale. The unique payload, the Atmospheric LAser Doppler INstrument (ALADIN), is a direct detection wind lidar operating at 355 nm from a 320 km orbit (Stoffelen et al., 2005; ESA, 2008; Reitebuch, 2012). The backscatter signals from particulate and molecular backscatter are received by two different spectrometers, that is, a Fizeau interferometer in the Mie channel, measuring particulate backscatter, and a spectrometer using a double-edge filter with two Fabry-Perot interferometers (FPIs) in the Rayleigh channel, measuring molecular backscatter. The novel combination of these two techniques, which was

25 not integrated in wind lidars before, enlarges the observational altitude range from ground to the lowermost 30 km of the atmosphere. It provides one component of the wind vector along the instrument LOS with a vertical resolution of 0.25 km to 2 km and a wind speed precision of 2 m s^{-1} to 4 m s^{-1} depending on altitude (Reitebuch, 2012). Furthermore, as the first high spectral resolution lidar in space (Ansmann et al., 2007; Flamant et al., 2008), ALADIN has the potential to globally monitor cloud and aerosol optical properties to contribute to climate impact studies as well.

30 In the frame of the Aeolus program, a prototype instrument called ALADIN Airborne Demonstrator (A2D) was developed at the German Aerospace Centre (DLR). Due to its representative design and operating principle, the A2D has provided valuable information on the validation of the measurement principle from realistic atmospheric signals before the satellite

launch. In addition, the A2D is expected to contribute to the optimization of the wind measurement strategies for the satellite instrument as well as to the improvement of wind retrieval and quality control algorithms during satellite operation (Durand et al., 2006; Reitebuch et al., 2009; Paffrath et al., 2009). As the first ever airborne direct detection wind lidar, A2D has been deployed in several ground and airborne campaigns over the last 12 years (Li et al., 2010; Marksteiner, 2013; Weiler, 2017;
5 Lux et al., 2018; Marksteiner et al., 2018).

Different instrument response calibration approaches have been studied using both measurement and simulation to characterize or rather calibrate the ALADIN Rayleigh channel (Tan et al., 2008; Dabas et al., 2008; Rennie et al., 2017). Currently, only measured Rayleigh response calibrations (MRRC) are used for the A2D (Marksteiner, 2013; Lux et al., 2018; Marksteiner et al., 2018). However, the atmospheric and instrumental variability coming along with an MRRC limits the
10 reliability and repeatability of A2D instrument response calibrations. Inspired by the calibration method used in the ALADIN level 2B processor (Dabas and Huber, 2017), the Simulated Rayleigh Response Calibration (SRRC) was developed to resolve these limitations. It is based on accurate theoretical model of FPI transmission function and the molecular Rayleigh backscatter spectrum. In this paper, the SRRC is introduced and its impact on the A2D wind retrieval is discussed and compared to results obtained with a measured response calibration. In section 2, different calibration approaches of double-edge FPIs are
15 introduced. Afterwards, the principle of an A2D SRRC is presented in Section 3. Section 4 gives an overview over the campaign and the dataset analysed in this paper, whereas Section 5 introduces the A2D SRRC, which is applied to data from a flight campaign in 2016, and discusses the corresponding wind results. Section 6 provides a statistical comparison of LOS wind velocity from A2D Rayleigh channel measurement, SRRC, and those from simultaneous CDL and dropsonde datasets. The comparison of instrument response calibration from A2D Rayleigh channel measurement and SRRC is also evaluated in
20 Section 6. Section 7 provides a summary and conclusions.

2 Calibration approaches for double-edge FPIs

Chanin et al. (Chanin et al., 1989) demonstrated for the first time that FPIs can be used to measure wind in the middle atmosphere relying on molecular Rayleigh scattering with a laser wavelength of 532 nm. The frequency-dependent response calibration, which can be defined as the contrast (Chanin et al., 1989) or the ratio (Korb et al., 1992) of the signal intensities
25 obtained after transmission through the FPIs, is a prerequisite for wind retrieval since it represents the relationship between measured quantity (e.g. intensity of the backscattered light) and the frequency shift which is induced by the Doppler effect. Generally, there are two approaches to determine the relationship between response and Doppler frequency shift, which is called response calibration profile. Table 1 lists existing FPIs-based direct detection wind lidar systems that are capable to measure wind information based on measurement approach or simulation approach.

2.1 Measurement approach

The first approach is based on measurements during which the laser beam is pointed into zenith direction while assuming that the vertical velocity of the probed atmospheric volume is negligible, i.e. no Doppler frequency shift is induced. Then, in order to obtain the measured response calibration profile, either the frequency of the laser transmitter is scanned over fixed FPIs
5 (Reitebuch et al., 2018; Lux et al., 2018; Marksteiner et al., 2018) or the cavity length of the FPIs is scanned while keeping the laser frequency locked (Dou et al., 2014).

Since the shape of the actual molecular Rayleigh backscatter spectrum is determined by the atmospheric temperature and pressure conditions (Tenti et al., 1974; Pan et al., 2004), the measured response calibration profile is only valid for a specific combination of temperature and pressure profiles. Regarding ground-based lidar systems, the calibration procedure can be
10 carried out frequently based on atmospheric condition (Dou et al., 2014; Liu et al., 2002), and it is reasonable to assume that temperature and pressure show only small variations with a negligible effect on the retrieved wind within a specific analysis period. However, for spaceborne or airborne lidar systems like ALADIN or the A2D, the variability in temperature and pressure would be one of the main sources of systematic errors for the Rayleigh channel wind retrieval as it modifies the instrument response calibration (Dabas et al., 2008; Marksteiner, 2013).

15 In terms of ALADIN, the Rayleigh winds produced by the level 1B processor (Reitebuch et al., 2018) are based on a measured atmospheric response calibration curve. A so-called instrument response calibration is usually performed once per week. During these about 16 minutes the frequency of the laser transmitter is scanned over ±500 MHz (around the cross point of the FPI) in steps of 25 MHz and the satellite is rolled by 35° in order to point nadir, thereby avoiding frequency shifts induced by horizontal wind velocities. Furthermore, in order to increase the signal to noise ratio (SNR), the signals from the
20 altitude range between 6 km and 16 km are accumulated to derive a single response calibration curve for the atmosphere (Reitebuch et al., 2018). Compared to ALADIN, the atmospheric Rayleigh response calibration of the A2D can be obtained and used per range-gate because of the larger SNR prevailing for airborne measurements being closer to their target. The instrument response calibration of the A2D can be carried out several times during a flight by tuning the laser frequency in steps of 25 MHz over a frequency interval of 1.7 GHz.

25 Apart from the atmospheric temperature and pressure effect on the measured response calibration profile, some experimental limitations and requirements need to be considered carefully to achieve a reliable instrument response calibration for both ALADIN and A2D. Firstly, because of the different spectral widths of the particle and molecular backscatter signal, the sensitivity of the FPIs on them are different, thus the Mie contamination on Rayleigh channel should be avoided to ensure the representativity of pure Rayleigh response. Furthermore, the ground condition, such as high albedo and preferably flat terrain
30 as well as low ground elevation, should be considered to improve the SNR, to facilitate the deduction of a ground return response curve and to maximize the vertical coverage of the atmosphere (Marksteiner, 2013; Weiler, 2017; Lux et al., 2018;

Atmospheric
Measurement
Techniques
Discussions

Marksteiner et al., 2018). In some cases, A2D calibrations were performed over terrain with high elevation (e.g. Greenland). Obviously, no response calibration curve can be obtained from below the surface, which would however be necessary for accurate wind retrieval at other geographical locations with lower ground elevation. In addition, the LOS velocity needs to be zero during the instrument response calibration. This is accomplished by flying curves with a roll angle of 20°, which

5 corresponds to the installation angle of the A2D telescope in the Falcon. Regions showing gravity wave activity or strong convection should be avoided as they cross the assumption of negligible vertical wind velocity (Lux et al., 2018; Marksteiner et al., 2018). Overall, the reliability and repeatability of ALADIN and A2D measured response calibration profile is a main limitation for accurate wind retrieval.

2.2 Simulation approach

10 The second approach is based on simulated response calibration profiles and the fact that the transmitted signals through each FPI are proportional to the convolution of the respective filter transmission function with the atmospheric backscatter spectrum. Therefore, this approach relies on accurate models for both FPI transmission functions and atmospheric backscatter spectrum. In practice, the transmission function of FPIs can be obtained by scanning laser frequency with fixed FPIs (Rennie et al., 2017) or scanning the spacing between the plates of FPIs with fixed laser frequency (Souprayen et al., 1999b; Xia et al., 2012).

15 In terms of ALADIN and A2D, the seed laser is frequency tuneable over a spectral range of 11 GHz to calibrate the spectral characteristics of FPIs for the internal reference path, and this procedure is called instrument spectral registration (Reitebuch et al., 2018). However, since the illumination of the FPIs can be different for the internal reference and the atmospheric path (Lux et al., 2018), the transmission functions of FPIs for the atmospheric path is slightly different compared to the one measured with the internal reference signal. For ALADIN, this is taken into account by correcting the FPIs transmission curves

20 for the atmospheric path (Dabas and Huber, 2017). Considering the limitation of A2D MRRC, an A2D SRRC based on this simulation approach promises an improvement in terms of A2D wind speed errors. The transmission function of A2D FPIs in the internal reference path can be obtained during instrument spectral registration. However, the determination of transmission characteristics of FPIs in atmospheric path of A2D is the most sophisticated part to accurately retrieve the wind information using SRRC. Furthermore, it should be noted that regardless of measurement or simulation method, any angular alignment

25 drift will change the incidence angles on FPIs, and hence change their transmission characteristics. This will result in a change of the response calibration that has to be considered to avoid systematic errors in wind retrieval. As for Observatory of Haute Provence (OHP) Rayleigh lidar, the bias induced by instrument drift can be eliminated based on quick wind acquisition cycle strategy, and the spectral drift can thus be removed by using the differences between vertical and tilted position profiles (Souprayen et al., 1999a). For ALADIN or A2D, the instrument drift is compensated by regularly performing instrument

30 response calibrations and instrument spectral registrations on a weekly basis.

3 The principle of A2D SRRC

The Doppler frequency shift in LOS direction is derived from the difference between the frequency of the received atmospheric return f_a and the emitted laser frequency f_i:

$$\Delta f = f_a - f_i , \tag{1}$$

5   The corresponding LOS velocity is derived from the Doppler shift equation using laser wavelength of λ_0:

$$V_{LOS} = \frac{\lambda_0}{2} \Delta f , \tag{2}$$

For each direct detection wind lidar system, the emitted laser frequency should be known to accurately derive the Doppler frequency shift. A zero Doppler shift reference determined by pointing to the zenith direction has been used to correct the short-term frequency drift in previous studies (Souprayen et al., 1999b; Korb et al., 1992; Dou et al., 2014). But for ALADIN
10   or A2D, the internal reference path is specially used to measure the emitted laser frequency information. In order to derive f_i and f_a from the A2D Rayleigh channel, the transmitted intensity $I_{A,B,INT}(f)$ and $I_{A,B,ATM}(f)$ through FPIs filter A and B for internal reference (INT) and atmospheric (ATM) paths are used, respectively:

$$I_{A,B,INT}(f_i) = \int_{-FSR/2}^{+FSR/2} T_{A,B,INT}(f) S_i(f) df , \tag{3}$$

$$I_{A,B,ATM}(f_a) = \int_{-FSR/2}^{+FSR/2} T_{A,B,ATM}(f) S_a(f) df , \tag{4}$$

15   $$S_a(f) = S_{RB}(f) + (\rho - 1) S_{mie}(f) , \tag{5}$$

where FSR is the free spectral range for the corresponding FPI (A or B) and measurement path (INT or ATM). Taking the transmitted intensity through filter A for instance, $I_{A,INT}(f_i)$ is the convolution of the filter A transmission function at internal reference path $T_{A,INT}(f)$ and the normalized laser reference spectrum $S_i(f)$ with transmitted laser frequency of f_i, and $I_{A,ATM}(f_a)$ is the convolution of filter A transmission function at atmospheric path $T_{A,ATM}(f)$ and the normalized atmospheric
20   backscatter signal spectrum $S_a(f)$ with backscattered signal centre frequency of f_a. $S_a(f)$ consists of the broad molecular Rayleigh backscatter spectrum $S_{RB}(f)$ (the subscript RB stands for Rayleigh–Brillouin) and the narrow particulate Mie backscatter spectrum $S_{mie}(f)$, as shown in Eq. (5), and $\rho = 1 + \beta_{aer} / \beta_{mol}$ is the scattering ratio, where β_{aer} and β_{mol} are the backscattered coefficients of particle and molecular, respectively.

As described in Garnier and Chanin (Garnier and Chanin, 1992), the Rayleigh responses for internal reference or
25   atmospheric paths are defined as:

Atmospheric
Measurement
Techniques
Discussions

$$R_x(f) = \frac{I_{A,x}(f) - I_{B,x}(f)}{I_{A,x}(f) + I_{B,x}(f)}, x = INT \text{ or } ATM ,$$

(6)

where x represents the case of internal reference (INT) or atmospheric (ATM) path calibration, respectively.

In order to determine the $R_x(f)$ by means of Eqs. (3)-(6), accurate knowledges about $T_{A,B,INT}(f)$, $T_{A,B,ATM}(f)$, $S_i(f)$ and $S_a(f)$ is needed. Generally, the transmission function $T(f)$ of an ideal FPI can be expressed by the Airy function, however,

5   small defects on the FPI mirror surface or of the illumination of the FPI could result in small deviations that have to be considered for an accurate analysis. It is shown that all these defects can be represented by a Gaussian defect term, modifying the model of the FPI transmission function $T(f)$ to (Witschas et al., 2012):

$$T(f) = \frac{1}{FSR}[1 + 2\sum_{k=1}^{\infty} R^k \cos(\frac{2\pi k f}{FSR})\exp(-\frac{2\pi^2 k^2 \sigma_g^2}{FSR^2})] ,$$

(7)

where R is the mean reflectivity of the mirror and σ_g is a defect parameter taking mirror defects into consideration.

10    $S_i(f)$ can be approximated by a Gaussian function for the laser pulse line shape with its laser linewidth parameter and frequency of emitted laser (Lux et al., 2018; Marksteiner et al., 2018). The spectral distribution of $S_{mie}(f)$ is similar to $S_i(f)$ as particles can be considered to cause no spectral broadening due to a random motion. $S_{RB}(f)$ can be computed by using the Tenti S6 line shape model (Tenti et al., 1974; Pan et al., 2004) which has been widely applied in atmospheric application. An easy-processable analytical representation of Tenti S6 line shape model for atmospherically relevant temperatures and

15   pressures is used herein (Witschas, 2011a, b; Witschas et al., 2014).

The particulate Mie scattering which is not fully filtered out by the Fizeau interferometer will enter the FPIs and can be considered as Mie contamination of the Rayleigh signal. The measurement principle of the A2D Rayleigh channel signal is shown in Fig. 1. It is assumed that there is no Mie contamination on Rayleigh channel in this case, that is, ρ=1 or $S_a(f)$=$S_{RB}(f)$. $S_i(f)$ is depicted using a Gaussian function with a full width at half maximum (FWHM) of 50 MHz. $S_{RB}(f)$

20   is calculated for T=270 K and p=700 hPa. The transmitted integrated intensities of $S_a(f)$ through FPIs A and B, that is, $I_{A,ATM}$ and $I_{B,ATM}$ are indicated by light blue and magenta filled areas, respectively.

The LOS wind velocity error induced by Mie contamination ΔV is defined as the difference of LOS wind velocity under pure atmospheric molecular condition and atmospheric spectral condition with scattering ratio of ρ. Figure 2 shows the simulation of ΔV at T=223 K and P=301 hPa, where the x-axis and y-axis represent different response values and scattering

25   ratios, respectively. Positive and negative ΔV represent the overestimation and underestimation of LOS velocity, respectively. An overestimate of LOS velocity occurs at response values less than 0.2, and larger scattering ratio results in larger

Atmospheric
Measurement
Techniques
Discussions

Open Access

EGU

overestimation. The difference can get up to 20 m s^{-1} in case of $\rho > 10$. Also, it is more severe when Mie signal is significant for the Rayleigh channel but not high enough to retrieve LOS velocity from the Mie channel accurately (Sun et al., 2014; Lux et al., 2018), which is the case for low scattering values, e.g. below 1.5.

5   Following the procedure of the A2D instrument response calibration mode, the transmitted intensities through FPIs and corresponding response values at each frequency scan step are calculated, eventually forming the SRRC of internal reference path ($R_{INT}(f)$, blue line) and atmospheric path ($R_{ATM}(f)$, black line) shown in Figure 3 (a). The cross point frequency f_c (red dot line) in Fig. 3 (a) is derived from $R_{INT}(f)$ where $I_{A,i}(f) - I_{B,i}(f)$ is closest to zero (Marksteiner et al., 2018). The relative frequency f' is defined as the difference between absolute frequency f and f_c. Figure 3 (b) shows the simulated $R_{INT}(f')$ and $R_{ATM}(f')$ within a relative frequency interval of ± 850 MHz, corresponding to the red-square marked frequency

10 area in Fig. 3 (a). A linear least-square fit is applied to the SRRC of the internal reference and atmospheric path with blue and black line shown in Fig. 3 (b). The linear fitting parameters including the sensitivity β_x and intercept α_x are defined as below:

$$\beta_x = \frac{\partial R_x(f')}{\partial f'}, x = INT \text{ or } ATM, \tag{8}$$

$$\alpha_x = R_x(f' = 0) = R_x(f = f_c), \tag{9}$$

The non-linearity $\gamma_x(f')$ is defined as the difference between $R_x(f')$ and linear least-square fitting result, that is,

15 $\gamma_x(f') = R_x(f') - (\beta_x f' + \alpha_x)$. As shown in Fig. 3 (c), the $\gamma_x(f')$ characterizations of the $R_{INT}(f')$ and $R_{ATM}(f')$ are clearly visible, especially for the case $R_{ATM}(f')$. For wavelength of $\lambda_0 = 354.89$ nm, a LOS velocity of 1 m s^{-1} translates to a frequency shift of 5.63 MHz (Lux et al, 2018). Taking the sensitivity $\beta_{ATM} = 5 \times 10^{-4}$ MHz^{-1} for example, the atmospheric non-linearity at -200 MHz can be up to nearly -0.02 shown in Fig. 3 (c), which is equivalent to magnitudes of up to -40 MHz corresponding to -7.1 m s^{-1}. Large errors in the derived LOS velocity would occur if $\gamma_x(f')$ is not taken into account.

20 Therefore, a 5th order polynomial fit (Marksteiner, 2013; Lux et al., 2018; Marksteiner et al., 2018) is selected to model $\gamma_x(f')$, as shown in Fig. 3 (c) for $R_{INT}(f')$ ($R_{ATM}(f')$) in blue (black) line. Then the fitting SRRC for internal reference and atmospheric path can be expressed as:

$$R_{fit,x}(f') = \beta_x f' + \alpha_x + \gamma_{fit,x}(f') = \beta_x f' + \alpha_x + \sum_{i=0}^{5} m_{i,x} f'^i$$

$$= (a_x + m_{0,x}) + (\beta_x + m_{1,x})f' + m_{2,x}f'^2 + m_{3,x}f'^3 + m_{4,x}f'^4 + m_{5,x}f'^5, \tag{10}$$

Atmospheric
Measurement
Techniques
Discussions

The difference between $R_x(f^{'})$ and $R_{fit,x}(f^{'})$ is defined as response residual as shown in Fig. 3 (d) for the internal reference path (blue line) and atmospheric path (black line), respectively. A periodic fluctuation can be seen but the maximum residual of atmospheric path is less than 1.5×10^{-4}, corresponding to 0.053 m s^{-1} for β_{ATM} =5×10^{-4} MHz^{-1}.

4 Campaign and dataset

5   In the frame of the North Atlantic Waveguide and Downstream Experiment (NAWDEX) carried out in 2016 in Iceland, four aircraft equipped with diverse payloads were employed to investigate the influence of diabatic processes for midlatitude weather (Schäfler et al., 2018). The DLR Falcon 20 was deployed with the A2D and a well-established 2 μm CDL, offering an ideal platform to demonstrate the feasibility of the A2D under complex dynamic conditions. All in all 14 research flights were performed with the Falcon aircraft during the NAWDEX campaign. The wind measurement mode of A2D was operated in
10 most of the flight periods, and the instrument spectral registration mode was also carried out during ground tests and airborne measurements. Furthermore, two flights on September 28th 2016 and October 15th 2016 were carried out to obtain A2D instrument response calibration. Six MRRCs have been performed in these two calibration flight periods. After comparison and evaluation given by Lux et al. (Lux et al., 2018), it is concluded that the 3rd calibration, which is carried out over an Iceland glacier on 12:53 UTC September 28th 2016, is chosen as the baseline of A2D Rayleigh wind retrieval, as it shows low Rayleigh
15 residual errors and was not affected by clouds, instrument temperature drifts and other outliers (Lux et al., 2018). The other three aircraft, that is, the German High Altitude and Long Range Research Aircraft (HALO), the French Service des Avions Français Instrumentés pour la Recherche en Environnement (SAFIRE) Falcon 20 and the British Facility for Airborne Atmospheric Measurements (FAAM) BAe 146, were equipped with dropsonde dispensers to provide temperature, pressure, wind and humidity profiles (Schäfler et al., 2018). Time-space matching datasets between dropsonde and A2D can not only
20 be used as reference to validate A2D wind measurements, but also offer essential atmospheric temperature and pressure profiles for SRRC in this study. Table 2 provides an overview of datasets during 2016 campaign flight used for this study. It is noted that all matched dropsondes listed in Table 2 were dispensed from the HALO aircraft.

It is noted that the transmission functions of the FPIs are reproducible, and the transmission characteristics are different for the internal reference and atmospheric path due to slightly different illumination properties of the different optical paths. As
25 for the A2D instrument spectral registration during the NAWDEX campaign, the sampled transmission function of the FPIs is obtained from the internal reference path rather than the atmospheric path, as the atmospheric return is convolved with RB spectrum and the hard target return is too variable due to albedo variation. The only available sampled transmission functions of the FPIs from atmospheric path for A2D was carried out in 2009 during the BRillouin scattering Atmospheric INvestigation on Schneefernerhaus (BRAINS) field campaign (Witschas, 2011c; Witschas et al., 2012), which was performed during Jan-
30 Feb 2009 to demonstrate the effect of Brillouin scattering in real atmosphere. Unique at BRAINS was that a horizontal

alignment of the outgoing laser beam was used to get a hard target return of a mountain with constant albedo for the atmospheric path at about a distance of 10 km. Therefore, a narrowband backscatter signal through the atmospheric path was measured. The transmission functions of the FPIs were sampled by changing the laser frequency with steps of 50 MHz over a frequency range of 12 GHz with fixed FPIs. Different transmission curves of FPIs from the BRAINS field campaign in 2009 and

5   NAWDEX airborne campaign in 2016 will be used as candidate FPIs transmission curves for SRRC analysis herein.

5 Determination of the A2D response function and Rayleigh wind retrieval

A flowchart of the LOS wind velocity retrieval based on SRRC and MRRC is presented in Fig. 4. Firstly, the atmospheric temperature and pressure profiles are taken from dropsonde, radiosonde or model data to derive the atmospheric molecular backscattered spectrum using the analytical representation of Tenti S6 line shape model (Witschas, 2011a, b; Witschas et al.,

10 2014). Then the transmission functions of FPIs are obtained by fitting the measured FPIs transmission characteristics based on Eq. (7). After the determination of the atmospheric molecular backscatter spectrum and the transmission functions of the FPIs, the frequency scan of the laser transmitter during A2D instrument response calibration is simulated to derive the SRRC for the internal reference and the atmospheric path, respectively. The measured response values obtained from A2D wind velocity measurement mode are brought into the fitted SRRC $R_{fit,ATM}(f')$ and $R_{fit,INT}(f')$. The Doppler frequency shift Δf_{SRRC} due to

15 LOS velocity is then derived from the difference of $f'_{a,SRRC}$ and $f'_{i,SRRC}$ (Reitebuch et al., 2018):

$$\Delta f_{SRRC} = f'_{a,SRRC} - f'_{i,SRRC} = \frac{R_{fit,ATM}(f'_{a,SRRC}) - \alpha_{ATM} - \gamma_{fit,ATM}(f'_{a,SRRC})}{\beta_{ATM}} - \frac{R_{fit,INT}(f'_{i,SRRC}) - \alpha_{INT} - \gamma_{fit,INT}(f'_{i,SRRC})}{\beta_{INT}}, \qquad (11)$$

The LOS velocity $V_{LOS,SRRC}$ is derived using the Doppler shift equation:

$$V_{LOS,SRRC} = \frac{\lambda_0}{2} \Delta f_{SRRC}, \qquad (12)$$

It is noted that LOS velocity herein includes not only the component from horizontal wind but also the contribution from

20 the aircraft flight velocity. The correction of the flight-induced velocity $V_{LOS,aircraft}$ is calculated using the inertial navigation system, GPS on-board the aircraft and attitude correction algorithm (Marksteiner, 2013). Finally, the corrected LOS wind velocity $V_{cor,SRRC}$ is obtained as follows:

$$V_{cor,SRRC} = V_{LOS,SRRC} - V_{LOS,aircraft}, \qquad (13)$$

5.1 Transmission characteristics of FPIs from different campaigns

A least-square nonlinear procedure is applied to each sampled transmission function obtained from BRAINS field campaign in 2009 and NAWDEX airborne campaign in 2016, respectively. Figure 5 illustrates the fits of the transmission functions

5 where the intensities are normalized to the maximum of filter A. The black one is derived from ground-based atmospheric path (ATMG) measurement during BRAINS field campaign in 2009. The red and blue curves are obtained from the ground-based internal reference path (INTG) and airborne internal reference path (INTA) measurement during NAWDEX campaign in 2016, respectively. The specific parameters of FPIs are listed in Table 3. The difference between ATMG and INTG is due to the different illumination of the FPI for the atmospheric and internal reference optical paths. Also, the measurement shown by the

10 INTA is broader than INTG's, which is most likely due to a slight contamination by atmospheric signal which is not completely blocked within the A2D optical receiver.

5.2 Determination of FPIs transmission functions for SRRC

The most critical part both for ALADIN and for the A2D Rayleigh response calibration is the determination of transmission curves of the FPIs for the internal reference and atmospheric paths, respectively. As for ALADIN, plate defects have to be

15 considered which lead to an asymmetric modification of the FPI transmission function in the atmospheric path. Thus, the FPIs transmission curve in the atmospheric path is modelled by a convolution of an Airy function, which describes the transmission of a perfect FPI, and a tilted top-hat function (Witschas, 2011c; Dabas and Huber, 2017). The core idea of this corrected spectral registration using Airy and top-hat function is based on the comparison of predicted and MRRC. The FPIs transmission characteristics cannot represent the actual sensitivity of the Rayleigh receiver at the atmospheric path until the difference of

20 predicted and the measured responses coincide within a threshold limit.

Different from ALADIN, the A2D FPIs transmission curves both in the internal reference path and in the atmospheric path were measured in previous campaigns. As listed in Table 4, 5 combinations of FPIs transmission functions derived from different campaigns are used to derive different SRRCs. Since there is no simultaneous dropsonde measurement to provide atmospheric temperature and pressure information for modelling the atmospheric molecular backscattered spectrum during the

25 3rd calibration, the radiosonde dataset at a distance of about 229 km to the calibration region (available at: http://weather.uwyo.edu/upperair/sounding.html) is used. The sensitivity β_x and intercept α_x from fitting SRRCs can give a qualitative comparison with the A2D MRRC. According to Eq. (11), the partial derivative of α_x and β_x can be obtained as follows:

$$\frac{\partial \Delta f}{\partial \alpha_{ATM}} = -\frac{\Delta \alpha_{ATM}}{\beta_{ATM}},$$
(14)

$$\frac{\partial \Delta f}{\partial \alpha_{INT}} = \frac{\Delta \alpha_{INT}}{\beta_{INT}} , \tag{15}$$

$$\frac{\partial \Delta f}{\partial \beta_{ATM}} = \frac{\alpha_{ATM} - A}{\beta_{ATM}^2} \Delta \beta_{ATM} , A \equiv R_{ATM} - \gamma_{ATM} , \tag{16}$$

$$\frac{\partial \Delta f}{\partial \beta_{INT}} = \frac{B - \alpha_{INT}}{\beta_{INT}^2} \Delta \beta_{INT} , B \equiv R_{INT} - \gamma_{INT} , \tag{17}$$

Using the typical values in the previous studies (Lux et al., 2018), that is, $\beta_{ATM} = 5.8 \times 10^{-4}$ MHz^{-1}, $\beta_{INT} = 4.5 \times 10^{-4}$ MHz^{-1},

5   $\alpha_{ATM} = $ -0.06 , $\alpha_{INT} = -0.001$,   and assuming $\Delta \beta_{ATM} = 10^{-5}$ MHz^{-1}, $\Delta \beta_{INT} = 10^{-5}$ MHz^{-1}, $\Delta \alpha_{ATM} = 0.01$ and $\Delta \alpha_{INT} = 0.01$,

which are realistic or rather probable to occur, it can be seen that the change of intercept $\Delta \alpha_{ATM}$ or $\Delta \alpha_{INT}$ results in frequency

differences of about -17 MHz or 22 MHz, equivalent to velocity differences of -2.99 m s^{-1} or 3.91 m s^{-1}, respectively. The

effect of sensitivity $\Delta \beta_{ATM}$ or $\Delta \beta_{INT}$ on velocity is related to the value of A or B. In the case of A=0 or B=0, the change of

sensitivity $\Delta \beta_{ATM}$ or $\Delta \beta_{INT}$ result in frequency difference of about -1.8 MHz or 0.05 MHz, equivalent to velocity differences

10   of -0.31 m s^{-1} or 0.009 m s^{-1}. Therefore, the retrieval of LOS wind velocity is more susceptible to intercept than sensitivity.

The responses of internal reference (red) and one atmospheric range gate (blue, herein 8th is chosen, for instance) from

measurement and corresponding SRRCs are listed in Table 4 and shown in Fig. 6. Generally, compared to the intercept of the

ATM response as shown by the blue dashed line (-0.059), the 1st and 3rd combination shown in Fig. 6 (a) (c) are underestimated

(-0.068, -0.102, respectively), while the 2nd and 4th combination shown in Fig. 6 (b) (d) are overestimated (-0.040, -0.042,

15   respectively). Only the 5th combination, shown in Fig. 6 (e) where the FPI parameters obtained from INTA and ATMG are

used for internal reference and atmospheric response determination, shows the similar intercept value (-0.055). In order to

further determine which combination matches best to the actual measured Rayleigh calibration response, the procedure adopted

in ALADIN (Dabas and Huber, 2017) is used. Herein, ε_R is defined as the difference between response from the respective

SRRCs and the measured response calibration. Then, the linear fit of ε_R as function of f' is made, returning a slope and

20   intercept based on Eqs. (18A) – (18B) in (Dabas and Huber, 2017). Basically, if the result from the SRRC matches the measured

response calibration, the slope and intercept should be as close to 0 as possible. Table 4 also lists the fitting results using 5

different combinations, and it is shown that the 5th combination has second smallest absolute slope and offset, offering the

overall consistence with the measured case. Therefore, the 5th combination will be used for initial SRRC determination.

5.3 Optimization of FPIs transmission characterization

25   The comparison of sensitivity and intercept of response calibration, as well as the LOS wind velocity derived from SRRC and

A2D measurements, can intuitively assess the feasibility of SRRC on A2D Rayleigh wind retrieval. Figure 7 (a) (b) shows the

comparison of β_{ATM} and $\Delta \alpha_{ATM} = \alpha_{ATM} + m_{0,ATM}$ between results from SRRC and A2D Rayleigh channel measurement at

08:33:06 UTC on 23 September 2016, respectively. The LOS wind velocity results from SRRC, MRRC, simultaneous

Atmospheric
Measurement
Techniques
Discussions

dropsonde measurements and CDL measurements are presented in Fig. 7 (c). It can be seen that β_{ATM} and $\Delta\alpha_{ATM}$ derived from SRRC have the similar altitude dependence as the one derived from MRRC, indicating the atmospheric temperature and pressure effect on the response calibration is described correctly within the SRRC. However, the discrepancy of $\Delta\alpha_{ATM}$ between results from SRRC and measured RRC shown in Fig. 7(b) is obvious, resulting in large discrepancy on LOS wind

5 velocity between SRRC and A2D Rayleigh channel datasets shown in Fig. 7(c). Taking data from a dropsonde which was released from HALO at the same location as reference, the LOS results from SRRC is underestimated at a height of 1 km – 8 km where it can be regarded as "clear" Rayleigh wind without Mie contamination, assuming that no aerosols are prominent in this altitude. Thus, a further optimization of FPIs parameters needs to be implemented as the stability of the optical alignment of the instrument can remarkably influence the performance of the A2D (Reitebuch et al., 2009; Lemmerz et al., 2017; Lux et

10 al., 2018).

Considering the optical path of the A2D Rayleigh channel, the FPI centre frequency is sensitive to the incidence angle of the light. It is a reasonable way to optimize FPI transmission function by fine adjusting the centre frequency of filter A or B for the atmospheric path. Assuming the centre frequencies of filter A and B have the same offset Δf_0 compared to the values obtained from ATMG, that is, $\Delta f_0 = \Delta f_{0,A} = \Delta f_{0,B}$, and the FPIs parameters at internal reference path are regarded as ideal,

15 Figs. 8(a) and 8(b) present the effect of Δf_0 on the sensitivity and intercept of fitting SRRC at each range gate, respectively. A cost function $F(\Delta f_0)$ is defined to determine the optimized centre frequency as follows:

$$F(\Delta f_0) = \sum_{i=1}^{N} |V_{LOS,SRRC}(i) - V_{LOS,reference}(i)|, \qquad (18)$$

where $V_{LOS,SRRC}(i)$ is the LOS wind velocity derived from SRRC with centre frequency offset of Δf_0 at range gate i, $V_{LOS,reference}(i)$ is the LOS wind velocity from simultaneous dropsonde datasets interpolated to the height of A2D Rayleigh

20 channel range gate i. Herein all available range gates from $i = 1$ to $i = N$ are used to calculate the cost function $F(\Delta f_0)$ for different Δf_0.

It can be seen from Fig. 8 (c) that $F(\Delta f_0)$ has its minimum when the centre frequencies of both filter A and B for the atmospheric path increase by 20 MHz, corresponding to the optimization case for LOS wind velocity retrieval using SRRC. The profiles for β_{ATM} and $\Delta\alpha_{ATM}$ derived from SRRC with FPIs optimization are shown in Fig. 9 (a) and (b), respectively.

25 Consistent with Figs. 8(a) and 8(b), the increase of centre frequency of filter A and B ($\Delta f_0 > 0$) results in decrease of β_{ATM} and $\Delta\alpha_{ATM}$. As shown in Fig. 9 (c), the LOS wind velocity derived from SRRC with optimized FPIs parameters fits quite well to the dropsonde results except for heights below 1 km and at around 9 km where Mie contamination may negatively influence the results.

6 Statistical comparison and assessment

The statistical comparisons of LOS wind velocities derived from SRRC with other instrument measurements are required to assess the feasibility and robustness of SRRC under various atmospheric conditions. Firstly, the quality control based on an SNR mask derived from the A2D Mie channel is applied (Marksteiner, 2013) to identify invalid winds retrieved from the

5   Rayleigh channel, retaining a significant amount of valid Rayleigh winds which were rejected by a cloud and ground mask (Lux et al., 2018). Then, based on the matched dates listed in Table 2, the comparisons of LOS wind velocity from dropsonde measurements, A2D Rayleigh channel measurements, and results derived from SRRC with and without FPI optimization are illustrated in Fig. 10, respectively. A linear fit to the data points is presented to provide the slope and intercept. The correlation coefficient, bias and standard deviation are also calculated and listed in Table 5. Fig. 10 (a) illustrates the comparison of LOS

10   wind velocity between dropsonde and A2D Rayleigh channel measurement, showing that the fitting parameters slightly deviate from the ideal case. The bias and standard deviation of A2D Rayleigh winds are 0.23 m s^{-1} and 2.20 m s^{-1}, respectively, which is comparable to results in previous studies (Lux et al., 2018). The comparison of LOS wind velocity between dropsonde measurements and the results derived from SRRC without FPIs optimization is illustrated in Fig. 10 (b). The corresponding bias and standard deviation are determined to be -3.32 m s^{-1} and 2.61 m s^{-1}, respectively. It can be seen the underestimation of

15   LOS wind velocity from SRRC without FPIs optimization is significant, demonstrating the necessity of FPIs optimization before wind retrieval using SRRC procedure. Figure 10 (c) shows the comparison of LOS wind velocity between dropsonde measurements and results derived from SRRC with FPIs optimization. The bias is 0.05 m s^{-1}, which is better than the results from A2D wind with MRRC, and the standard deviation is 2.52 m s^{-1}, comparable to the results from A2D Rayleigh wind retrieval, implying the feasibility and robustness of SRRC with FPIs optimization on A2D Rayleigh wind retrieval. From now

20   on, only SRRC results with optimized FPI parameters will be discussed.

The atmospheric temperature affects the Rayleigh-Brillouin line shape, and has a direct effect on the SRRC (Dabas et al., 2008). Figure 11 (a) shows the atmospheric temperature difference between SRRC and MRRC, where the red square and blue bar represent the mean bias and standard deviation at each height. The difference of sensitivity and intercept of response calibration between SRRC and MRRC are also illustrated in Fig. 11 (b) (c). It can be seen from Fig. 11 (a) that larger

25   discrepancies of atmospheric temperature can be found at about 7 km to 8 km with mean differences of less than 5 K. But for the corresponding differences of sensitivity and intercept shown in Fig. 11 (b) (c), larger discrepancies appear in lower heights, especially at heights lower than 3 km. On the one hand, it is implied that the atmospheric temperature effect is less significant in the statistical analysis of 2016 flight campaign. However, the temperature difference between MRRC and the actual wind measurement must be considered as an important source of wind bias for the case with large temperature difference. This is

30   the reason why it is mandatory to correct temperature for Aeolus wind retrieval in order to retrieve reliable winds (Dabas et al., 2008; Rennie et al., 2017). On the other hand, due to the ground elevation limitation during A2D instrument response calibration, the measured response calibration below 2 km in this case cannot be obtained, thus the measured response

calibration at height of 2 km are used for LOS velocity retrieval below 2 km, causing larger discrepancies shown in Fig. 11 (b) (c).

The height-dependent comparisons of LOS wind velocity from different datasets after quality control are illustrated in Fig. 12. The mean difference of LOS wind velocity between SRRC and A2D Rayleigh channel measurements shown in Fig. 12 (a)

5 has opposite trend at lower and higher heights, which is related to the intercept difference shown in Fig. 9 (b). Similar LOS wind velocity difference tendency can be seen in Fig. 12 (b) (c) for the case between SRRC and dropsonde, and between A2D Rayleigh channel measurement and dropsonde, respectively. Generally, larger discrepancies occur at heights of smaller than 2 km and larger than 8 km. The LOS wind velocities derived from A2D Rayleigh channel measurements have more obvious discrepancies at heights smaller than 2 km compared to the results derived from SRRC, consistent to the results shown in Fig.

10 11 and 12 that inappropriate values of A2D calibration parameters at lower height result in additional LOS velocity bias, and this is one of the limitations of A2D Rayleigh response calibration which can be overcome using SRRC. In order to analyse the height-dependent deviations more comprehensively, Fig. 13 shows the examples of LOS wind velocity from A2D Rayleigh channel measurement, dropsonde measurements, SRRC and CDL on 23 September 2016, where dropsonde and CDL are interpolated to the A2D height. Larger discrepancies can be obviously seen at heights larger than 8 km due to the occurrence

15 of cloud layer in these cases. Based on Eq. (5), when the Mie narrow spectrum with scattering ratio larger than 1 adds to the pure molecular Rayleigh-Brillouin line shape, the Rayleigh response calibration is affected directly, resulting in unrealistic LOS velocities and large systematic errors.

All matched CDL observations listed in Table 2 are used to assess the probability of Mie contamination on Rayleigh wind results. Figure 14 (a) shows the CDL measurement behaviour where valid (or invalid) signal is represented as 1 (or 0). The

20 Mie contamination fraction F_{Mie}, shown in Fig. 14 (b), is defined as the ratio of the number of valid signals to all CDL observation number N (here $N=12$) at each height. Obviously, the F_{Mie} at heights of smaller than 2 km and between 7 km and 11 km have much higher values and thus are mostly experienced by the Mie contamination compared to other heights, giving the important cause why larger discrepancies occur at height of less than 2 km and larger than 8 km shown in Fig. 12 and 13. It is also implied that even though quality control mentioned above is used, it cannot guarantee the accurate removal of

25 Rayleigh wind affected by Mie contamination. Indeed, the Mie contamination correction is another strength of SRRC. However, a detailed discussion is beyond the scope of this paper.

7 Summary and conclusion

As the first ever airborne direct detection wind lidar, the A2D has been deployed in several ground and airborne campaigns over the last 12 years for validating the measurement principle of Aeolus and further improving the algorithm and measurement

30 strategy. The A2D instrument calibration is used to obtain the response calibration profile indicating the relationship between

Atmospheric
Measurement
Techniques
Discussions

the measured signal intensities and the Doppler frequency shift which is proportional to the wind speed. However, the atmospheric and instrumental variability currently limit the reliability and repeatability of the A2D instrument response calibration. For instance, there are some factors affecting the accuracy of response calibration directly during instrument response calibration such as Mie contamination, non-zero vertical velocity, and unavailable response at lower elevation

5   because of the elevation limitation during instrument response calibration. The Simulated Rayleigh Response Calibration (SRRC) is thus presented in this paper to overcome these limitations of measured response calibration, further demonstrating the availability and merits of SRRC.

The most critical part of SRRC is the determination of the transmission characteristics of FPIs for the internal reference and atmospheric paths, respectively. Different from the method used for the determination of ALADIN FPIs transmission curve in

10   the atmospheric path where a tilted top-hat function is used, the A2D candidate SRRCs using different combinations of FPIs transmission characteristics obtained from different campaigns were calculated and compared to the measured Rayleigh response firstly. It is found that the combination of FPI parameters obtained from airborne internal reference path measurement and the ground-based atmospheric path measurement are the best to be used for the internal reference and atmospheric response determination by SRRC. Since the stability of the optical properties of the FPIs and the optical alignment of the instrument

15   can remarkably influence the performance of the A2D, a fine tuning of FPIs centre frequency for atmospheric path is performed to optimize the SRRC parameters. It is concluded that when the centre frequencies of both filter A and B at atmospheric path are increase by 20 MHz, the LOS wind velocity derived from SRRC provides the best consistency with dropsonde reference measurements. It is noted that the dropsonde is the reference quantity in this study to get an optimized SRRC, and it is also potential to use other reference such as ECMWF model dataset and 2 μm CDL.

20   Dropsonde data was used as a reference for statistical comparison of LOS wind velocity since it has the generally best spatiotemporal matching and coverage with SRRC. Firstly, the biases of LOS wind velocity derived from SRRC without and with FPIs optimization are -3.32 m s^{-1} and 0.05 m s^{-1}, respectively, showing the necessity of FPIs optimization for SRRC wind retrieval. Then the LOS wind velocity from SRRC with FPIs optimization shows that the standard deviation is 2.52 m s^{-1}, showing better accuracy and comparable precision compared to the results obtained from a conventional (measured) Rayleigh

25   response calibration yielding a bias of 0.23 m s^{-1} and standard deviation of 2.20 m s^{-1}, thus demonstrating the feasibility and robustness of SRRC on A2D Rayleigh wind retrieval. Furthermore, the height-dependent statistical comparison shows that the biases caused by inappropriate calibration parameters below 2 km due to the limitation of elevation during A2D instrument response calibrations can be overcame using SRRC, where the simulation of response values over the whole altitude range from the aircraft down to mean sea level can be achieved. The larger biases at heights of below 2 km and above 8 km are

30   probably related to the Mie contamination on the Rayleigh channel. It is also shown that even though quality control based on SNR is used, it cannot guarantee the accurate removal of the points affected by Mie contamination. This shows the necessity of combination of Mie and Rayleigh channel wind analysis.

Overall, the SRRC allows correcting for the atmospheric temperature and pressure profiles, and the possible ground elevation limitations and can, hence, improve the accuracy of A2D wind measurements especially at lower altitudes. It can improve the reliability and repeatability limitations caused by atmospheric and instrumental variability and constraints during A2D instrument response calibration measurement. Further studies based on A2D SRRC will be performed regarding the atmospheric temperature/pressure effect, Mie contamination correction and the particulate optical properties retrieval.

References

Ansmann, A., Wandinger, U., Le Rille, O., Lajas, D., and Straume, A. G.: Particulate backscatter and extinction profiling with the spaceborne high-spectral-resolution Doppler lidar ALADIN: methodology and simulations, Appl. Opt., 46, 6606-6622, https://doi.org/10.1364/AO.46.006606, 2007.

Baker, W. E., Atlas, R., Cardinali, C., Clement, A., Emmitt, G. D., Gentry, B. M., ... & Ma, Z.: Lidar-measured wind profiles: The missing link in the global observing system, Bulletin of the American Meteorological Society, 95(4), 543-564, , 2014.

Baumgarten, G.: Doppler Rayleigh/Mie/Raman lidar for wind and temperature measurements in the middle atmosphere up to 80 km, Atmos. Meas. Tech., 3, 1509-1518, https://doi.org/10.5194/amt-3-1509-2010, 2010.

Bruneau, D.: Mach–Zehnder interferometer as a spectral analyzer for molecular Doppler wind lidar, Appl. Opt., 40, 391-399, https://doi.org/10.1364/AO.40.000391, 2001.

Bruneau, D., and Pelon, J.: Simultaneous measurements of particle backscattering and extinction coefficients and wind velocity by lidar with a Mach–Zehnder interferometer: principle of operation and performance assessment, Appl. Opt., 42, https://doi.org/10.1364/AO.42.001101, 1101-1114, 2003.

Chanin, M. L., Garnier, A., Hauchecorne, A., and Porteneuve, J.: A Doppler lidar for measuring winds in the middle atmosphere, Geophys. Res. Lett., 16, 1273-1276, https://doi.org/10.1029/GL016i011p01273, 1989.

Dabas, A., Denneulin, M. L., Flamant, P., Loth, C., Garnier, A., and Dolfi-Bouteyre, A.: Correcting winds measured with a Rayleigh Doppler lidar from pressure and temperature effects, Tellus A: Dyn. Meteorol. Oceanogr., 60, 206-215, https://doi.org/10.1111/j.1600-0870.2007.00284.x, 2008.

Dabas, A., and Huber, D.: Generation and update of AUX_CSR, AE-TN-MFG-L2P-CAL-003, 4.0, 43 pp, 2017.

5 Dou, X., Han, Y., Sun, D., Xia, H., Shu, Z., Zhao, R., Shangguan, M., and Guo, J.: Mobile Rayleigh Doppler lidar for wind and temperature measurements in the stratosphere and lower mesosphere, Opt. Express, 22, A1203-A1221, https://doi.org/10.1364/OE.22.0A1203, 2014.

Durand, Y., Chinal, E., Endemann, M., Meynart, R., Reitebuch, O., and Treichel, R.: ALADIN airborne demonstrator: a Doppler Wind lidar to prepare ESA's ADM-Aeolus Explorer mission, in: Proceedings of Earth Observing Systems XI.
10 International Society for Optics and Photonics, San Diego, California, United States, September 2006.

ESA.: ADM-Aeolus: Science Report, ESA Communication Production Office, 2008.

Flamant, P., Cuesta, J., Denneulin, M. L., Dabas, A., and Huber, D.: ADM-Aeolus retrieval algorithms for aerosol and cloud products, Tellus A: Dyn. Meteorol. Oceanogr., 60, 273-286, https://doi.org/10.1111/j.1600-0870.2007.00287.x, 2008.

Flesia, C., and Korb, C. L.: Theory of the double-edge molecular technique for Doppler lidar wind measurement, Appl.
15 Opt., 38, https://doi.org/10.1364/AO.38.000432, 432-440, 1999.

Flesia, C., Korb, C. L., & Hirt, C.: Double-edge molecular measurement of lidar wind profiles at 355 nm, Opt. Lett., 25, 1466-1468, https://doi.org/10.1364/OL.25.001466, 2000.

Garnier, A., and Chanin, M. L.: Description of a Doppler Rayleigh lidar for measuring winds in the middle atmosphere, Appl. Phys. B, 55, 35-40, https://doi.org/10.1007/BF00348610, 1992.

20 Herbst, J., and Vrancken, P.: Design of a monolithic Michelson interferometer for fringe imaging in a near-field, UV, direct-detection Doppler wind lidar, Appl. Opt., 55(25), 6910-6929, https://doi.org/10.1364/AO.55.006910, 2016.

Hildebrand, J., Baumgarten, G., Fiedler, J., Hoppe, U. P., Kaifler, B., Lübken, F. J., and Williams, B. P.: Combined wind measurements by two different lidar instruments in the Arctic middle atmosphere, Atmos. Meas. Tech., 5, 2433-2445, https://doi.org/10.5194/amt-5-2433-2012, 2012.

25 Korb, C. L., Gentry, B. M., and Weng, C. Y.: Edge technique: theory and application to the lidar measurement of atmospheric wind, Appl. Opt., 31, 4202-4213, https://doi.org/10.1364/AO.31.004202, 1992.

Korb, C. L., Gentry, B. M., Li, S. X., and Flesia, C.: Theory of the double-edge technique for Doppler lidar wind measurement, Appl. Opt., 37, 3097-3104, https://doi.org/10.1364/AO.37.003097, 1998.

Lemmerz, C., Lux, O., Reitebuch, O., Witschas, B., and Wührer, C.: Frequency and timing stability of an airborne injection-seeded Nd: YAG laser system for direct-detection wind lidar, Appl. Opt., 56, 9057-9068, https://doi.org/10.1364/AO.56.009057, 2017.

Li, Z., Lemmerz, C., Paffrath, U., Reitebuch, O., and Witschas, B.: Airborne Doppler lidar investigation of sea surface reflectance at a 355-nm ultraviolet wavelength, J. Atmos. Oceanic Technol., 27, 693-704, https://doi.org/10.1175/2009JTECHA1302.1, 2010.

Liu, Z. S., Wu, D., Liu, J. T., Zhang, K. L., Chen, W. B., Song, X. Q., Hair, J. W., and She, C. Y.: Low-altitude atmospheric wind measurement from the combined Mie and Rayleigh backscattering by Doppler lidar with an iodine filter, Appl. Opt., 41, 7079-7086, https://doi.org/10.1364/AO.41.007079, 2002.

Lux, O., Lemmerz, C., Weiler, F., Marksteiner, U., Witschas, B., Rahm, S., Schäfler, A., and Reitebuch, O.: Airborne wind lidar observations over the North Atlantic in 2016 for the pre-launch validation of the satellite mission Aeolus, Atmos. Meas. Tech., 11, 3297-3322, https://doi.org/10.5194/amt-11-3297-2018, 2018.

Marksteiner, U.: Airborne wind lidar observations for the validation of the ADM-Aeolus instrument, Ph.D. thesis, Technische Universität München, 176 pp., 2013.

Marksteiner, U., Lemmerz, C., Lux, O., Rahm, S., Schäfler, A., Witschas, B., and Reitebuch, O.: Calibrations and Wind Observations of an Airborne Direct-Detection Wind LiDAR Supporting ESA's Aeolus Mission, Remote Sens., 10, 2056, https://doi.org/10.3390/rs10122056, 2018.

McKay, J. A.: Modeling of direct detection Doppler wind lidar. II. The fringe imaging technique. Appl. Opt., 37, 6487-6493, https://doi.org/10.1364/AO.37.006487, 1998.

McKay, J. A.: Assessment of a multibeam Fizeau wedge interferometer for Doppler wind lidar, Appl. Opt., 41, 1760-1767, https://doi.org/10.1364/AO.41.001760, 2002.

Pan, X., Shneider, M. N., and Miles, R. B.: Coherent Rayleigh-Brillouin scattering in molecular gases. Phys. Rev. A, 69, 033814, https://doi.org/10.1103/PhysRevA.69.033814 , 2004.

Paffrath, U., Lemmerz, C., Reitebuch, O., Witschas, B., Nikolaus, I., and Freudenthaler, V.: The airborne demonstrator for the direct-detection Doppler wind lidar ALADIN on ADM-Aeolus. Part II: Simulations and Rayleigh Receiver Radiometric performance, J. Atmos. Oceanic Technol., 26, 2516-2530, https://doi.org/10.1175/2009JTECHA1314.1, 2009.

Atmospheric
Measurement
Techniques
Discussions

Reitebuch, O., Lemmerz, C., Nagel, E., Paffrath, U., Durand, Y., Endemann, M., Fabre. F., and Chaloupy, M.: The airborne demonstrator for the direct-detection Doppler wind lidar ALADIN on ADM-Aeolus. Part I: Instrument design and comparison to satellite instrument, J. Atmos. Oceanic Technol., 26, 2501-2515, https://doi.org/10.1175/2009JTECHA1309.1, 2009.

5 Reitebuch, O.: Wind Lidar for Atmospheric Research, in: Atmospheric physics: Background, methods, trends, edited by: Schumann, U., Research Topics in Aerospace, Springer, Berlin, London, 487–507, 2012.

Reitebuch, O., Huber, D., and Nikolaus, I.: ADM-Aeolus Algorithm Theoretical Basis Document (ATBD) Level1B Products, AE-RPDLR-L1B-001, 4.4, 117 pp., 2018.

Rennie, M., Tan, D., Andersson, E., Poli, P., Dabas, A., Kloe, J. D., Marseille, G. J., Stoffelen, A.: Aeolus Level-2B Algorithm
10 Theoretical Basis Document, AE-TN-ECMWF-L2BP-0023, 3.0, 109 pp., 2017.

Schäfler, A., Craig, G., Wernli, H., Arbogast, P., Doyle, J. D., McTaggart-Cowan, R., Methven, J., Rivière, G., Ament, F., Boettcher, M., Bramberger, M., Cazenave, Q., Cotton, R., Crewell, S., Delanoë, J., Dörnbrack, A., Ewald, F., Fix, A., Gray, S. L., Grob, H., Groß, S., Hagen, M., Harvey, B., Hirsch, L., Jacob, M., Kölling, T., Konow, H., Lemmerz, C., Lux, O., Magnusson, L., Mayer, B., Mech, M., Moore, R., Pelon, J., Quinting, J., Rahm, S., Rapp, M., Rautenhaus, M.,
15 Reitebuch, O., Reynolds, C. A., Sodemann, H., Spengler, T., Vaughan, G., Wendisch, M., Wirth, M., Witschas, B., Wolf, K., and Zinner. T.: The north atlantic waveguide and downstream impact experiment, Bull. Am. Meteorol. Soc., 99, 1607-1637, 2018.

She, C. Y., Yue, J., Yan, Z. A., Hair, J. W., Guo, J. J., Wu, S. H., and Liu, Z. S.: Direct-detection Doppler wind measurements with a Cabannes–Mie lidar: A. Comparison between iodine vapor filter and Fabry–Perot interferometer methods, Appl.
20 Opt., 46, 4434-4443, https://doi.org/10.1364/AO.46.004434, 2007.

Souprayen, C., Garnier, A., Hertzog, A., Hauchecorne, A., and Porteneuve, J.: Rayleigh–Mie Doppler wind lidar for atmospheric measurements. I. Instrumental setup, validation, and first climatological results, Appl. Opt., 38, 2410-2421, https://doi.org/10.1364/AO.38.002410, 1999a.

Souprayen, C., Garnier, A., and Hertzog, A.: Rayleigh–Mie Doppler wind lidar for atmospheric measurements. II. Mie
25 scattering effect, theory, and calibration, Appl. Opt., 38, 2422-2431, https://doi.org/10.1364/AO.38.002422, 1999b.

Stoffelen, A., Pailleux, J., Källén, E., Vaughan, J. M., Isaksen, L., Flamant, P., Wergen, W., Andersson, E., Schyberg, H., Culoma, A., Meynart, R., and Ingmannt, P.: The atmospheric dynamics mission for global wind field measurement, Bull. Am. Meteorol. Soc., 86, 73-88, https://doi.org/10.1175/BAMS-86-1-73, 2005.

Atmospheric
Measurement
Techniques
Discussions

Sun, X. J., Zhang, R. W., Marseille, G. J., Stoffelen, A., Donovan, D., Liu, L., and Zhao, J.: The performance of Aeolus in heterogeneous atmospheric conditions using high-resolution radiosonde data, Atmos. Meas. Tech., 7, 2695-2717, https://doi.org/10.5194/amt-7-2695-2014, 2014.

Tan, D. G., Andersson, E., Kloe, J. D., Marseille, G. J., Stoffelen, A., Poli, P., Denneulin, M. L., Dabas, A., Huber, D.,
5   Reitebuch, O., Flamant, P., Le Rille, O., and Nett, H.: The ADM-Aeolus wind retrieval algorithms, Tellus A: Dyn. Meteorol. Oceanogr., 60, 191-205, https://doi.org/10.1111/j.1600-0870.2007.00285.x, 2008.

Tenti, G., Boley, C. D., and Desai, R. C.: On the kinetic model description of Rayleigh–Brillouin scattering from molecular gases, Can. J. Phys., 52, 285-290, https://doi.org/10.1139/p74-041, 1974.

Thuillier, G., and Hersé, M.: Thermally stable field compensated Michelson interferometer for measurement of temperature
10   and wind of the planetary atmospheres, Appl. Opt., 30, 1210-1220, https://doi.org/10.1364/AO.30.001210, 1991.

Tucker, S. C., Weimer, C. S., Baidar, S., and Hardesty, R. M.: The Optical Autocovariance Wind Lidar. Part I: OAWL Instrument Development and Demonstration, J. Atmos. Oceanic Technol., 35, 2079-2097, https://doi.org/10.1175/JTECH-D-18-0024.1, 2018.

Wang, Z., Liu, Z., Liu, L., Wu, S., Liu, B., Li, Z., and Chu, X.: Iodine-filter-based mobile Doppler lidar to make continuous
15   and full-azimuth-scanned wind measurements: data acquisition and analysis system, data retrieval methods, and error analysis, Appl. Opt., 49, 6960-6978, https://doi.org/10.1364/AO.49.006960, 2010.

Weiler, F.: Bias correction using ground echoes for the airborne demonstrator of the wind lidar on the ADM-Aeolus mission, Master's thesis, University of Innsbruck, 96 pp., available at: https://resolver.obvsg.at/urn:nbn:at:at-ubi:1-7104 (last access: 11 October 2017), 2017.

20   Weissmann, M., and Cardinali, C.: Impact of airborne Doppler lidar observations on ECMWF forecasts, Q. J. R. Meteorolog. Soc., 133, 107-116, https://doi.org/10.1002/qj.16, 2007.

Witschas, B.: Analytical model for Rayleigh–Brillouin line shapes in air, Appl. Opt., 50, 267-270,https://doi.org/10.1364/AO.50.000267, 2011a.

Witschas, B.: Analytical model for Rayleigh–Brillouin line shapes in air: errata, Appl. Opt., 50, 5758-5758,
25   https://doi.org/10.1364/AO.50.005758, 2011b.

Witschas, B.: Experiments on spontaneous Rayleigh-Brillouin scattering in air, PhD thesis, Friedrich-Schiller-Universität, Jena, 112 pp., available at: http://elib.dlr.de/98547/ (last access: 8 March 2017), 2011 (c).

Witschas, B., Lemmerz, C., and Reitebuch, O.: Horizontal lidar measurements for the proof of spontaneous Rayleigh–Brillouin scattering in the atmosphere, Appl. Opt., 51, 6207-6219, https://doi.org/10.1364/AO.51.006207, 2012.

Witschas, B., Lemmerz, C., and Reitebuch, O.: Daytime measurements of atmospheric temperature profiles (2–15 km) by lidar utilizing Rayleigh–Brillouin scattering, Opt. Lett., 39, 1972-1975,https://doi.org/10.1364/OL.39.001972, 2014.

5   Xia, H., Dou, X., Sun, D., Shu, Z., Xue, X., Han, Y., Hu, D., Han, Y., and Cheng, T.: Mid-altitude wind measurements with mobile Rayleigh Doppler lidar incorporating system-level optical frequency control method, Opt. Express, 20, 15286-15300, https://doi.org/10.1364/OE.20.015286, 2012.

Žagar, N., Stoffelen, A., Marseille, G. J., Accadia, C., and Schlüssel, P.: Impact assessment of simulated Doppler wind lidars with a multivariate variational assimilation in the tropics, Mon. Weather Rev., 136, 2443-2460,
10   https://doi.org/10.1175/2007MWR2335.1, 2008.
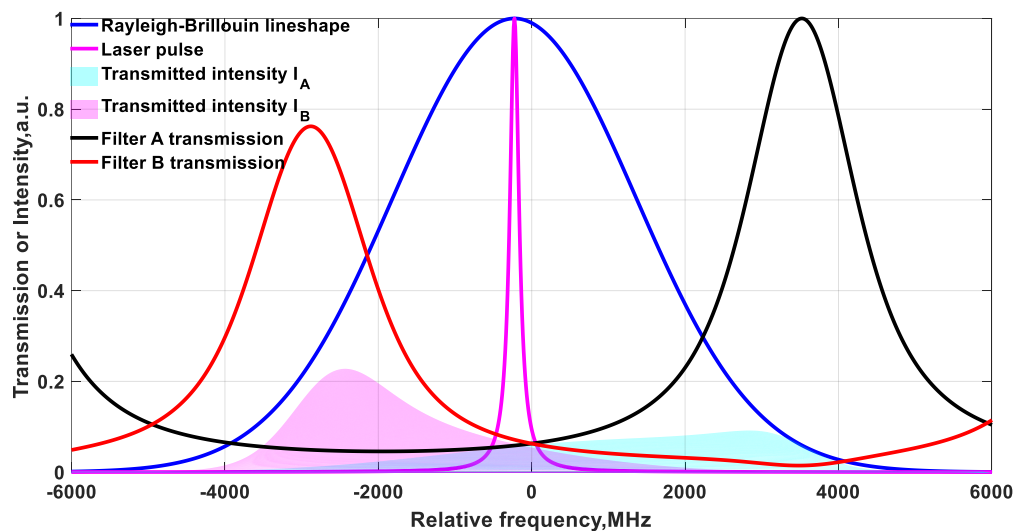
Figure 1: Modelled spectral distribution of the transmitted laser pulse (pink line) and pure molecular backscatter (blue line) for T=270 K, P=700 hPa normalized to one. The Rayleigh channel transmission spectra of two FPIs are shown in black T_A (*f*) and red T_B (*f*) lines, respectively. The transmitted integrated intensities through FPI A and B are marked with light blue and magenta filled areas.
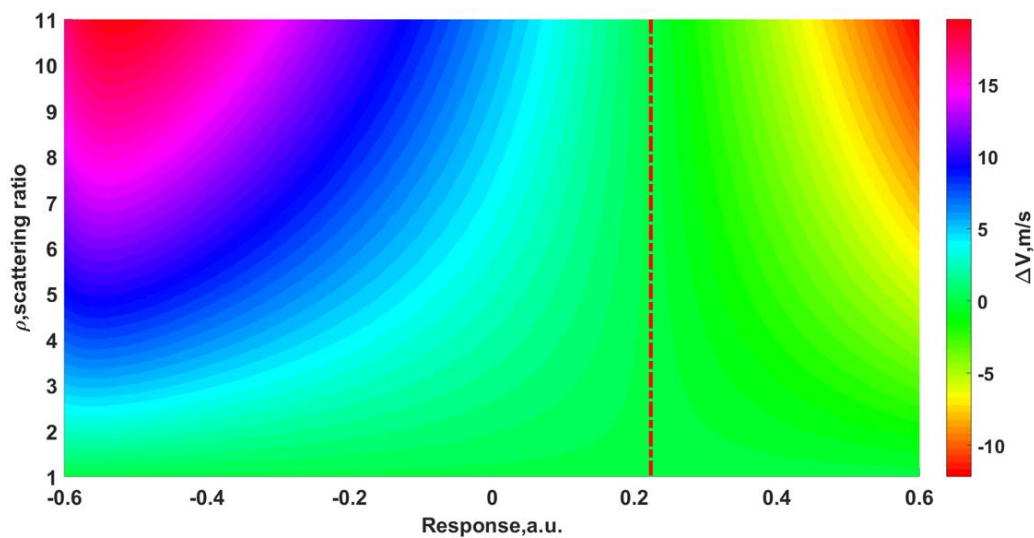
Figure 2: Simulation of LOS wind velocity errors ΔV generated by Mie contamination at T=223 K and P=301 hPa. The *x*-axis and *y*-axis represent the response value and scattering ratio ρ, respectively. The red dashed-line corresponds to the response value with minimum ΔV at each scattering ratio.

23
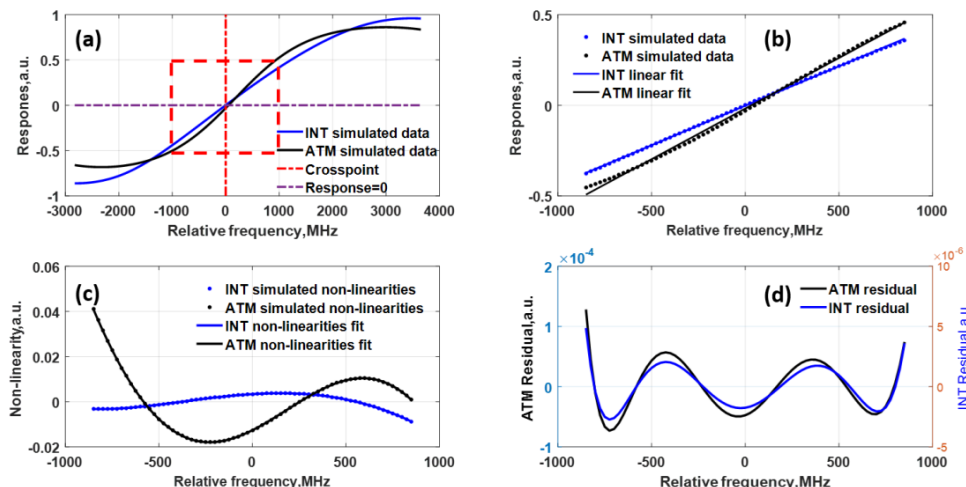
Figure 3: (a) The Simulated Rayleigh Response Calibration (SRRC) for internal reference (INT, blue line) and atmospheric return (ATM, black line), the cross point frequency is marked with red dot-line, (b) INT (blue dots) and ATM (black dots) response and corresponding linear least squares fit (blue line for INT, black line for ATM) calibration with a frequency interval of ±850 MHz, where relative frequency is used instead of absolute frequencies, (c) the non-linearities of simulated (dots) and fitted (lines) response functions from INT (blue) and ATM (black). (d) response function residuals from INT (blue line) and ATM (black line).
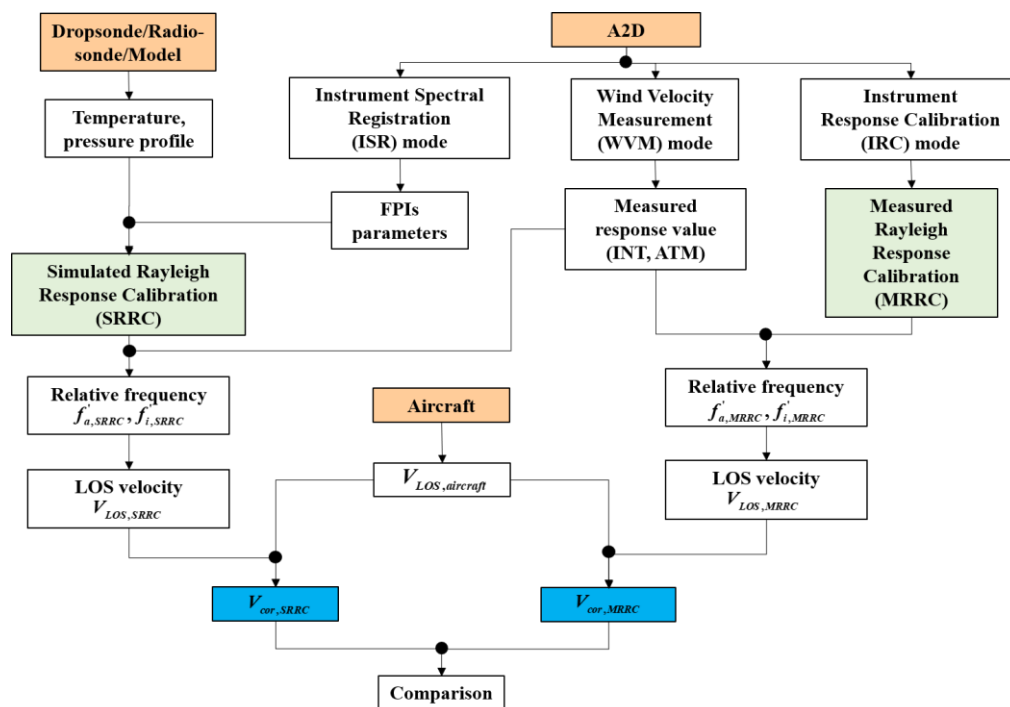
Figure 4: Flowchart of LOS velocity retrieval and comparison between A2D SRRC and MRRC.
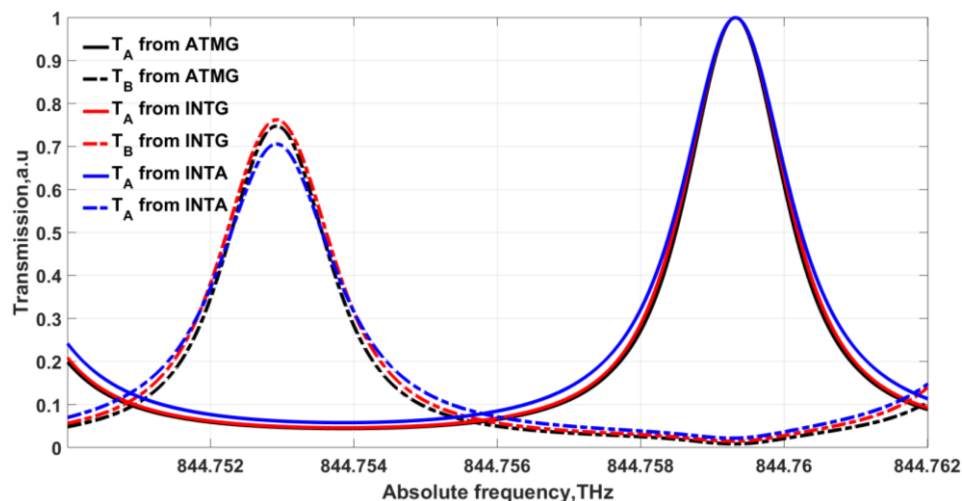
Figure 5: The transmission function fitting of FPIs from different campaigns and detection channels. The black, red and blue groups are obtained from ATM path measurement during BRAINS ground campaign (ATMG) in 2009, INT path measurement during NAWDEX from ground (INTG) in 2016 and INT path measurement during NAWDEX airborne measurement (INTA) in 2016, respectively.
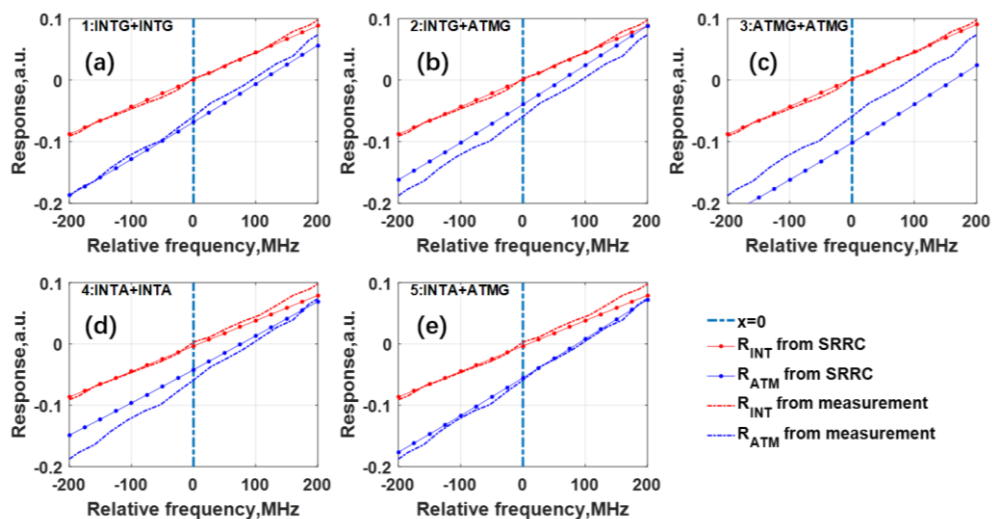

Figure 6: The response functions of internal reference and 8th atmospheric range gate from MRRC (red and blue dashed-lines, respectively) and different SRRCs using different combinations of FPIs transmission parameters (red and blue dot-lines, respectively) listed in table 4.
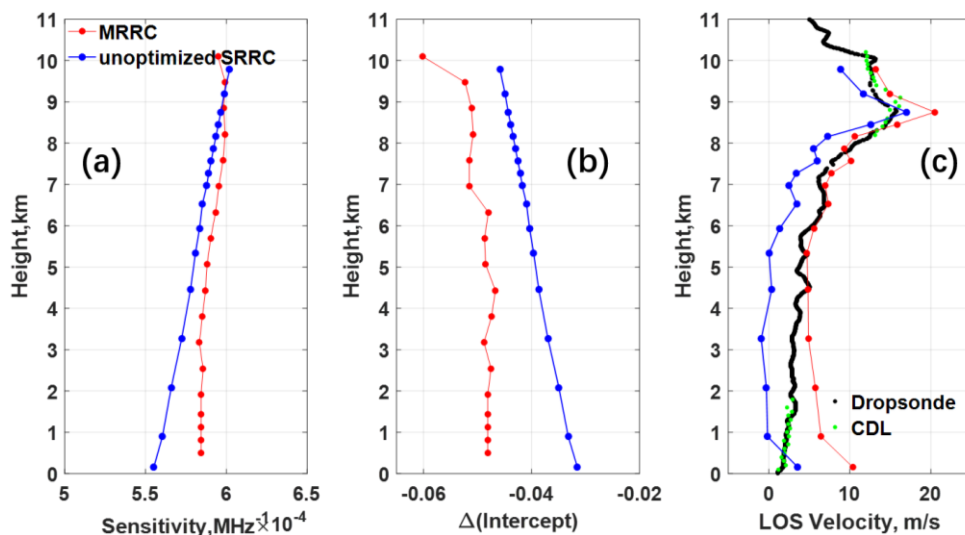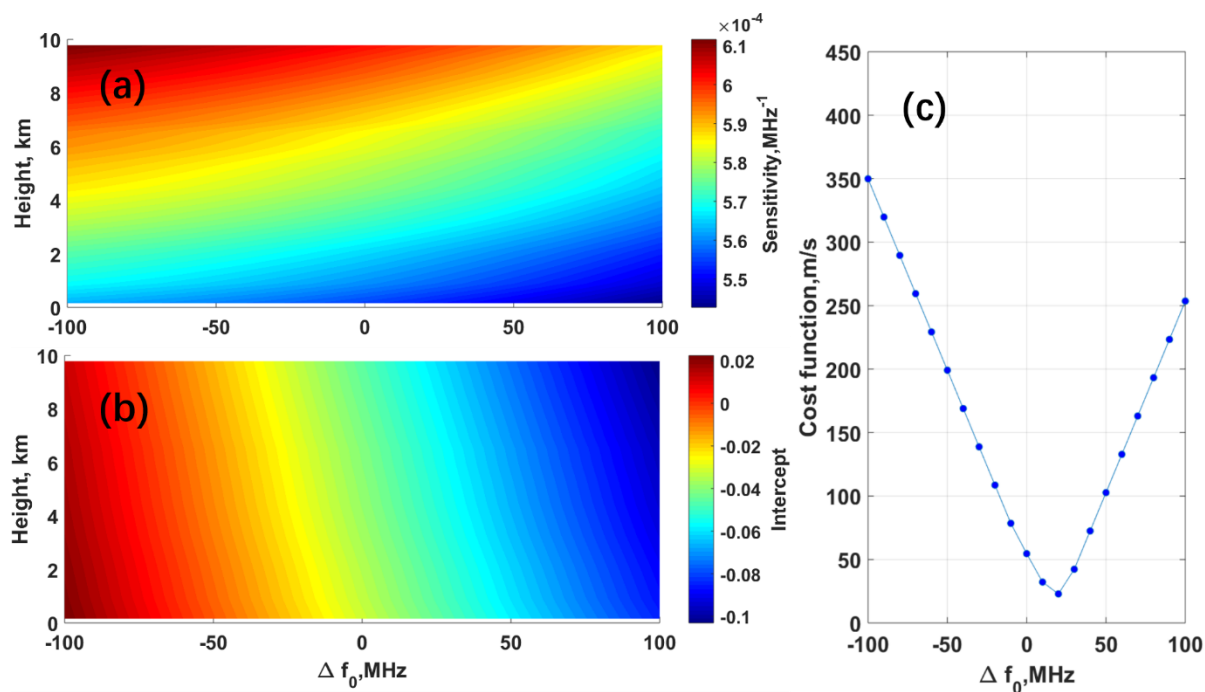
Atmospheric
Measurement
Techniques
Discussions

Figure 7: Case study using dropsonde data on 08:27:07 UTC, 23 September 2016: Comparison of (a) sensitivity (b) intercept (c) LOS velocity between results from A2D Rayleigh channel MRRC (red) and unoptimized SRRC (blue). The LOS velocity from dropsonde (black) and CDL (green) are also presented in Fig. 7 (c).

Figure 8: The effect of the centre frequency offset Δf_0 of filter A and B for atmospheric path on atmospheric response (a) β_{ATM} (b) $\Delta\alpha_{ATM}$ and (c) corresponding cost function $F(\Delta f_0)$.
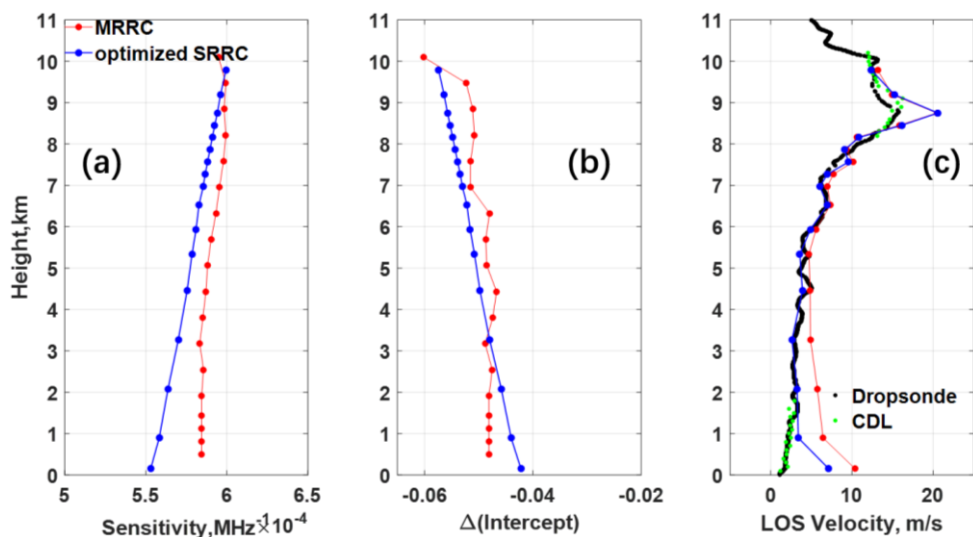
Figure 9: Case study using dropsonde data on 08:27:07 UTC, 23 September 2016: Comparison of (a) sensitivity (b) intercept (c) LOS velocity between results from A2D Rayleigh channel MRRC (red) and optimized SRRC (blue). The LOS velocity from dropsonde (black) and CDL (green) are also presented in Fig. 9 (c).
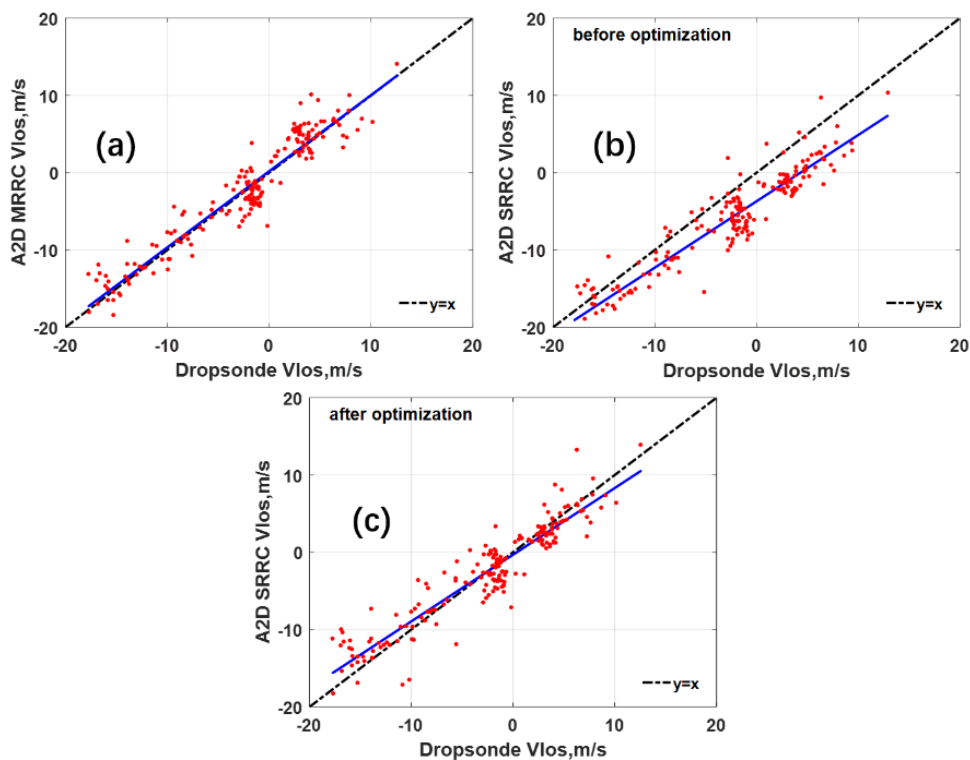

Figure 10: LOS velocity comparison obtained from (a) dropsonde and A2D Rayleigh channel measurement with MRRC (b) dropsonde and SRRC before FPIs optimization and (c) dropsonde and SRRC after FPIs optimization.
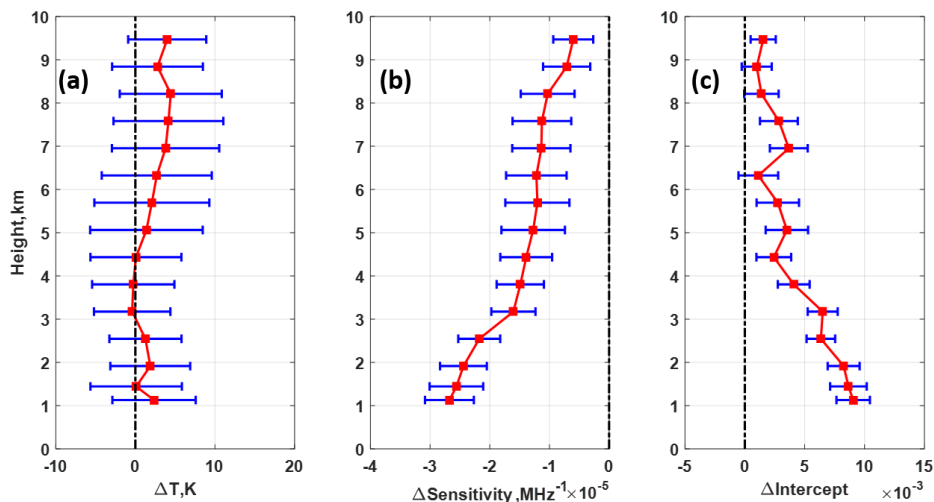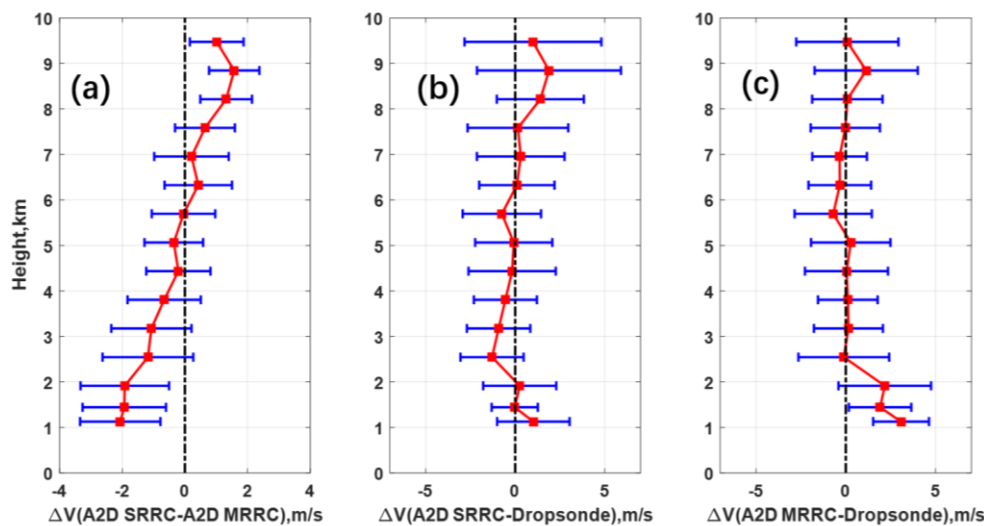
Figure 11: (a) Difference of temperature between dropsondes used in SRRC and the one during A2D instrument response calibration, and the difference of (b) sensitivity (c) intercept derived from A2D SRRC and MRRC. The red square and the blue bar represent the mean bias and standard deviation at each height.

Figure 12: The comparison profiles of LOS velocity (a) between A2D SRRC and MRRC (b) SRRC and dropsonde (c) MRRC and dropsonde.
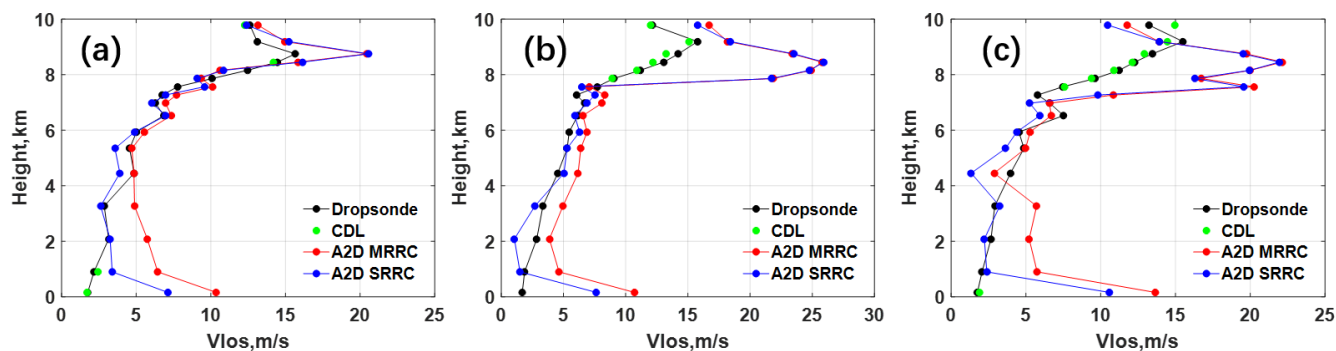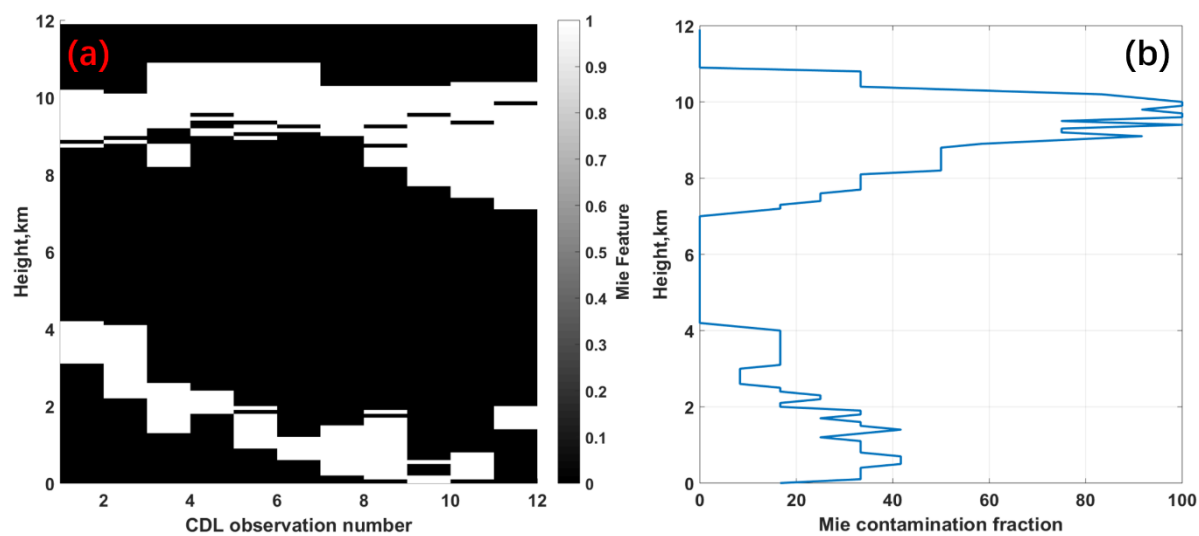
Figure 13: LOS velocity from dropsonde (black), CDL (green), A2D MRRC (red) and A2D SRRC (blue) on (a) 08:27:07 UTC (b) 08:33:06 UTC (c) 08:39:05 UTC, 23 September 2016.

5   **Figure 14: (a) Matched CDL measurement behaviour where valid (or invalid) signal is represented as 1 (or 0) (b) Mie contamination fraction F_{Mie} of selected datasets used for comparison analysis.**

Atmospheric
Measurement
Techniques

Open Access

EGU

Discussions

Table 1. Comparison of different FPI-based direct detection wind lidars

Lidar	Wavelength and system	Calibration approach	Instrument drift correction	References
OHP [a] Rayleigh lidar	532 nm, double FPIs	Simulation, FPI scanning	quick wind acquisition cycle strategy	Chanin et al., 1989; Garnier and Chanin, 1992; Souprayen et al., 1999a, 1999b
NASA [b] Rayleigh/Mie lidar	355 nm, three FPIs	Simulation FPI or laser scanning	locking etalon and servo-control system	Korb et al., 1992; Korb et al. 1998; Flesia and Korb, 1999; Flesia et al., 2000
USTC [c] Rayleigh lidar	355 nm, three FPIs	measurement and simulation, FPI scanning	locking etalon and servo-control system	Xia et al., 2012; Dou et al., 2014
ESA ALADIN	355 nm, double FPIs for Rayleigh channel	level 1B: measurement, laser scanning level 2B: simulation, laser scanning	internal reference path	Reitebuch et al., 2018; Rennie et al., 2017
DLR A2D	355 nm, double FPIs for Rayleigh channel	Measurement, laser scanning	internal reference path	Marksteiner, 2013; Lux et al., 2018; Marksteiner et al., 2018

[a] Observatory of Haute Provence, France

[b] National Aeronautics and Space Administration, U.S.

5   [c] University of Science and Technology of China, China. This lidar is mobile.

10

Atmospheric
Measurement
Techniques
Discussions

Table 2: Overview of analysed datasets from A2D, 2 μm CDL and dropsonde in the frame of the NAWDEX campaign.

Date	A2D measurement period (UTC) and mode	Data availability of CDL	Matched dropsonde Time (UTC)
17.09.2016	10:30-11:35 Wind measurement	available	11:09:15 11:33:47
	11:42-12:24 Wind measurement	no data	11:56:00 12:05:20 12:15:02 12:24:23
21.09.2016	15:34-15:57 Wind measurement	available	15:40:49 15:45:07 15:48:34 15:52:51
23.09.2016	07:51-08:53 Wind measurement	available	08:19:01 08:27:07 08:33:06 08:39:05 08:45:05 08:51:16
28.09.2016	12:53 - 13:17 Calibration	available	No data
18.10.2016	09:20-09:57 Wind measurement	not available	09:22:48 09:27:15 09:31:53 09:36:29 09:52:30

5

Atmospheric
Measurement
Techniques
Discussions

Table 3: Specific parameters of FPIs during different ground and airborne campaigns illustrated in Fig. 5

Parameters	ATM Ground ATMG		INT Ground INTG		INT Airborne INTA	
Filters	filter A	filter B	filter A	filter B	filter A	filter B
FSR (GHz)	10.934	10.998	10.934	10.851	10.934	10.934
FWHM (GHz)	1.671	1.733	1.743	1.847	1.833	1.943
R	0.670	0.696	0.668	0.679	0.622	0.610
σ_g (MHz)	266	363	303	391	210	247

Table 4: Combinations for internal reference and atmospheric response simulation with slope and intercept values of ε_R linear fit
5 **calculated based on Eqs. (18A) – (18B) (Dabas and Huber, 2017).**

Combination	Internal reference response	Atmospheric response	Slope	Intercept
1	INTG	INTG	-1.48×10^{-5}	-0.0057
2	INTG	ATMG	-1.42×10^{-7}	0.0206
3	ATMG	AMTG	-1.39×10^{-5}	-0.0356
4	INTA	INTA	-7.74×10^{-5}	0.0181
5	INTA	ATMG	-9.02×10^{-7}	0.0059

10

Atmospheric
Measurement
Techniques
Discussions

Table 5: Statistical comparison between results from dropsonde, A2D Rayleigh channel measurement and SRRC before and after FPIs optimization during 2016 campaign.

Statistical parameters	Dropsonde to A2D MRRC	Dropsonde to A2D SRRC before FPIs optimization	Dropsonde to A2D SRRC after FPIs optimization
Number of compared data pairs	185	190	190
Correlation coefficient	0.95	0.93	0.94
Slope	0.99	0.86	0.86
Intercept	0.19	-3.70	-0.32
Mean bias, m s^{-1}	0.23	-3.32	0.05
Standard deviation, m s^{-1}	2.20	2.61	2.52

5